Journal of Materials Chemistry

Cite this: J. Mater. Chem., 2012, 22, 20952

www.rsc.org/materials

PAPER

Nanoporous $LiMn_2O_4$ nanosheets with exposed {111} facets as cathodes for highly reversible lithium-ion batteries†

Weiwei Sun,[a] Feng Cao,[b] Yumin Liu,[a] Xingzhong Zhao,[a] Xiaogang Liu[c] and Jikang Yuan*[b]

Received 27th April 2012, Accepted 3rd July 2012
DOI: 10.1039/c2jm32658b

Control over porosity and exposed highly reactive facets is challenging in the area of materials science. Materials with high porosity and reactivity of exposed facets are favorable candidates in catalysis and energy storage. Here we demonstrate a facile template-free route to synthesize nanoporous $LiMn_2O_4$ nanosheets composed of single-crystalline $LiMn_2O_4$ nanorods with exposed {111} facets *via* an *in situ* lithiation of ultrathin MnO_2 nanosheets. Nearly 100% of the initial capacity can be retained after 500 cycles at a 1C discharge rate using the nanoporous nanosheets as a cathode, whereas at a discharge rate of 25C, the capacity retention is about 86% of the initial capacity after 500 cycles. The durable cycling performance and high capacity retention can be attributed to the intrinsic highly oriented crystallinity, two-dimensional (2D) nanoporosity and exposed {111} facet of the nanosheet cathode.

Introduction

Rechargeable lithium ion batteries (LIBs) have recently become one of the most significant and prospective candidates for reversible electrochemical energy storage devices.[1–3] Although great improvement has been made in the development of LIBs in commercial applications, challenging problems encountered when LIBs are used in electric vehicles (EVs) and hybrid electric vehicles (HEVs) cannot be easily mitigated.[4,5] Spinel-type $LiMn_2O_4$ is regarded as one of the most promising candidates for cathode materials in LIBs, owing to its inherent low-cost, environmental benignity, copious resource availability, and commendable safety.[6–8] However, the practical application of $LiMn_2O_4$ is hindered by problems such as capacity decay and poor cycling stability originating from the dissolution of Mn^{3+} *via* a disproportionation reaction in acid electrolytes and structural degradation during phase transition from cubic to tetragonal structure caused by Jahn-Teller distortion of MnO_6 octahedra within the $LiMn_2O_4$ lattice at higher current densities.[9–12] The strategies to retard the dissolution of manganese include surfacial modification and cation doping.[13–16] The poor cyclicity resulting from sluggish Li^+ ion diffusion in the bulk of $LiMn_2O_4$ can be improved using nanostructured cathodes,[17–20] because compared to their bulk counterparts, nanoscale dimension $LiMn_2O_4$ cathodes facilitate the Li^+ ion intercalation/deintercalation process through drastically shortened diffusion paths.[21–24]

Recently, enormous efforts have been made for the development of various nanostructured anodes and cathodes to improve their electrochemical performance in LIBs.[25–29] It is generally agreed that the electrochemical performance of electrodes strongly depends on their morphologies, crystallinity, and porosity. Xie *et al.*[25] and Imai *et al.*[26] found that three-dimensional (3D) architecture $LiMn_2O_4$ electrodes exhibit higher durability in the lithium insertion/extraction process at a high current density, owing to the short Li^+ ion diffusion lengths in the three-dimensional channels of the electrodes. Specifically, two-dimensional SnO_2 nanosheet anodes were reported to reveal faster Li^+ ion diffusion kinetics and superior high-rate capability owing to their two-dimensional (2D) geometry.[29] On the other hand, it was also reported that porous $LiMn_2O_4$ shows better rate capability and cycling ability compared to its counterparts that lack porosity, because the interconnected nanoporous framework could offer high accessibility for the electrolyte and preferably accommodate structural conversion during reduplicative Li^+ ion intercalation/deintercalation processes.[27,28] Further, it was reported that the formation of a solid electrolyte interface (SEI) on the surface of {111} planes of $LiMn_2O_4$ is critical and desirable for stabilizing its crystal structure during lithium ion insertion/desertion compared to other facets such as {110}, thus the development of $LiMn_2O_4$ with exposed {111} is highly desirable.

Herein, we report a novel method to prepare nanoporous $LiMn_2O_4$ nanosheets using (2D) ultrathin manganese dioxide nanosheets as precursor. To the best of our knowledge, this is the

[a]*School of Physics and Technology, Key Laboratory of Artificial Micro- and Nano-structure of Ministry of Education, Wuhan University, Wuhan, 430072, China*
[b]*Department of Applied Physics, The Hong Kong Polytechnic University, Hong Kong, China. E-mail: apjkyuan@inet.polyu.edu.hk; Fax: +852 2333 7629; Tel: +852 2766 5685*
[c]*Department of Chemistry, National University of Singapore, 117543, Singapore*

† Electronic supplementary information (ESI) available: other characterizations of products. See DOI: 10.1039/c2jm32658b

first time porous $LiMn_2O_4$ nanosheets composed of single crystalline $LiMn_2O_4$ with exposed {111} facets have been reported as cathodes for LIBs.

Experimental

Materials and synthesis

Ultrathin MnO_2 nanosheets were synthesized by a redox reaction of $HMnO_4$. The following equation shows the chemical reaction in our system:

$$3BaMnO_4(aq) + 3H_2SO_4(aq) = 2HMnO_4(l) + 3BaSO_4(s) + MnO_2(s) + 2H_2O(l)$$

$$HMnO_4(l) \xrightarrow{\text{copolymer}} MnO_2(s)$$

At first, $BaMnO_4$ (10 mmol) was dissolved in deionized water (90 ml) by continuous magnetic stirring to form a homogeneous solution. Then H_2SO_4 (2.4 ml, 4.23 M) was injected into the above solution, followed by a centrifugation to obtain fresh $HMnO_4$ solution. Meanwhile, ethanol (10 ml) was mixed with deionized water (60 ml), then block copolymer (11 ml, poly-(ethylene glycol)-block-poly(propylene glycol)-block-poly-(ethylene glycol), $M_W = 2900$) was dropped slowly into it by vigorous stirring to form a clear aqueous solution. After that, the fresh $HMnO_4$ solution was added dropwise to the block copolymer mixture solution with 10 r min^{-1} using a delivery pump under continuous magnetic stirring at room temperature. By means of vacuum degassing for 1 h, the obtained mixture solution was further stirred for 12 h to ensure a complete reaction of $HMnO_4$ solution. After the reaction, the black floccus MnO_2 nanosheet was filtered, and rinsed with ethanol and deionized water several times in order to remove soluble impurities. The product was dried in an oven at 100 °C overnight. The existence of copolymer in our synthetic system not only served as a template to facilitate two-dimensional growth of the MnO_2 nanosheets but also acted as a reducing agent taking part in the redox reaction of $HMnO_4$. The as-synthesized MnO_2 nanosheets (2.87 mmol) were subsequently added into diethyl ether (50 ml) under vigorous magnetic stirring for 1 h at room temperature to form a homogeneous mixture, and then lithium methide (1.07 ml, 1.6 M in diethyl ether) was transfused into this MnO_2 suspension dropwise followed by evaporation of the solvent at room temperature. The resulting solid power was transferred to a furnace and annealed at 700 °C for 4 h in nitrogen atmosphere, which resulted in porous single-crystalline $LiMn_2O_4$ nanosheets (PS-LMO). Just for comparison, $LiMn_2O_4$ was also synthesized as a counterpart through a conventional solid-state reaction (SS-LMO). The above-mentioned preparation process is also shown in Scheme 1.

Characterization of materials

The crystalline structures of the prepared MnO_2 nanosheets and PS-LMO nanosheets were identified by X-ray diffraction (XRD) using a Philips Xpert XRD system with Cu Ka radiation (λ = 1.54056 Å). The diffraction data were obtained at $2\theta = 10°–70°$, with a step size of 0.02°. The morphologies of the ultrathin MnO_2 nanosheets and PS-LMO nanosheets were observed by a field-emission scanning electron microscope (FESEM, JSM 6335F). TEM and HRTEM investigations were carried out using a JEOL 2010, equipped with an energy-dispersive X-ray analysis (EDX) system.

Scheme 1 Schematic representation of *in situ* conversion of ultrathin MnO_2 nanosheets to PS-LMO.

Electrochemical characterization

The electrochemical properties of the products were studied using 2032 coin-type half-cells that were assembled in a glove box filled with argon gas. We made the cathodes for the battery test cells from the active material (PS-LMO and SS-LMO), carbon black, and a poly(vinyl difluoride) binder in a weight ratio of 70 : 20 : 10. And then the cathode slurry was prepared by thoroughly mixing *N*-methyl-2-pyrrolidone (NMP) with the as-prepared active material, carbon black and poly(vinyl difluoride) binder. The blended slurry was then coated onto an aluminum foil current collector and dried at 80 °C for 12 h in a vacuum oven followed by roll-pressing. Finally, the entire assembly was dried under vacuum at 120 °C overnight. Pure lithium foil was employed as the anode and a polypropylene separator (Celgard) was used to separate the anode and cathode. The electrolyte consisted of a solution of 1.0 M $LiPF_6$ in ethylene carbonate (EC)/dimethyl carbonate (DMC) (1 : 1, in volume) obtained from Shenzhen Kejing Instrument Co. Ltd. The galvanostatic discharge and charge measurement were carried out on a Land test system in a voltage window of 3.2–4.3 V *vs.* Li/Li^+ at room temperature and with different rates. The cyclic voltammogram (CV) test was performed on CHI660C (ShangHai, China) electrochemistry workstation at a scan rate of 0.05 mV s^{-1} between 3.5 and 4.5 V *vs.* Li/Li^+.

Results and discussion

The phases of the precursor and the final product were identified by XRD (Fig. S1, ESI†). As seen in Fig. S1a,† all the peaks of (110), (211), (301), (600), and (002) can be assigned to the pure phase of MnO_2 (JCPDS no. 44-0141), whereas the XRD patterns of the obtained PS-LMO nanosheets (Fig. S1b†) are well indexed to a pure cubic spinel-type $LiMn_2O_4$ structure (JCPDS no. 35-0782).

The morphology of the MnO_2 nanosheets is examined by FE-SEM and FE-TEM (Fig. 1). As seen in Fig. 1a, the MnO_2 precursors consist of flower-like agglomerates made of intertangled ultrathin nanosheets with the dimension ranging from 100 nm to 200 nm in edge length. The formation of these two-dimensional (2D) nanosheets can be attributed to the usage of

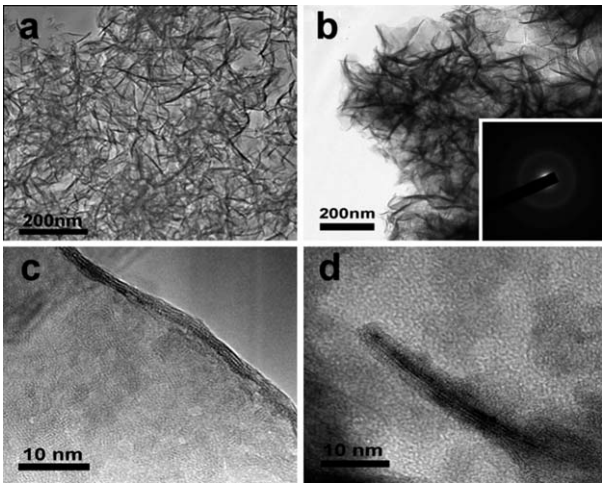

Fig. 1 (a) SEM image of ultrathin MnO_2 nanosheets, TEM images of (b) ultrathin MnO_2 nanosheets (the inset shows corresponding SAED pattern), (c) the edge of an individual MnO_2 nanosheet and (d) cross section of LiOH coated ultrathin MnO_2 nanosheet.

the block copolymer that serves as a morphology-directing and reduction agent for the nucleation and 2D growth of the MnO_2 nanosheets.[30] The TEM images of the MnO_2 nanosheets (Fig. 1b and c) confirm that the thickness of the nanosheets is less than 3 nm. As shown in the inset of Fig. 1b, the SAED (selected area electron diffraction) pattern supports the evidence of the poorly crystalline nature of the MnO_2 nanosheet previously confirmed by powder XRD characterization (Fig. S1a†). The TEM image (Fig. 1d) also shows a cross section of an individual MnO_2 nanosheet coated with a thin layer of LiOH with the thickness less than 5 nm.

Fig. 2 exhibits the SEM and TEM images of the as-synthesized products. The nano-structures of PS-LMO are revealed in Fig. 2a and b. Similarities between the morphologies of the precursor and final product confirm an *in situ* conversion during lithiation. The SEM image with high magnification shows that each nanostructured sheet is composed of small $LiMn_2O_4$ nanoparticles (Fig. 2b). The typical TEM image clearly reveals the nanoporous nature of PS-LMO, as shown in Fig. 2c. It is observed that each $LiMn_2O_4$ nanosheet consists of inter-connected nanorods, resulting in the formation of 2D nanopores with average pore size of approximately 100 nm (Fig. S2†). Formation of the nanoporous structure within the $LiMn_2O_4$ nanosheets probably arises from the volume shrinkage caused by oriented attachment and phase transition during the lithiation process of MnO_2 nanosheets at elevated temperature. The inset of Fig. 2c shows the high-magnification TEM image of PS-LMO. The HRTEM image (Fig. 2d) corresponds to the circled area marked in the inset of Fig. 2c. The measured neighbouring interplanar spacing of 0.48 nm, 0.41 nm and 0.29 nm can be indexed to the (111), (002), and (220) planes of $LiMn_2O_4$, respectively. Moreover, the corresponding selected area electron diffraction (SAED) patterns (the inset of Fig. 2d) present well-defined spots that can be well indexed to the (220), (111) and (002) planes of cubic spinel $LiMn_2O_4$ (JCPDS no. 35-0782), respectively. The single crystalline nature of the PS-LMO can also be confirmed by SAED. Further energy-dispersive X-ray analysis (EDX) results confirm the presence of both Mn and O elements in the $LiMn_2O_4$ nanosheets (Fig. S3†).

To further investigate the structural features of PS-LMO, it is reasonable to look into the TEM images of randomly selected particles in PS-LMO nanosheets, which are shown in Fig. 3a and b. The higher-magnification TEM images (Fig. 3c and d) correspond to the circled areas marked in Fig. 3a and b,

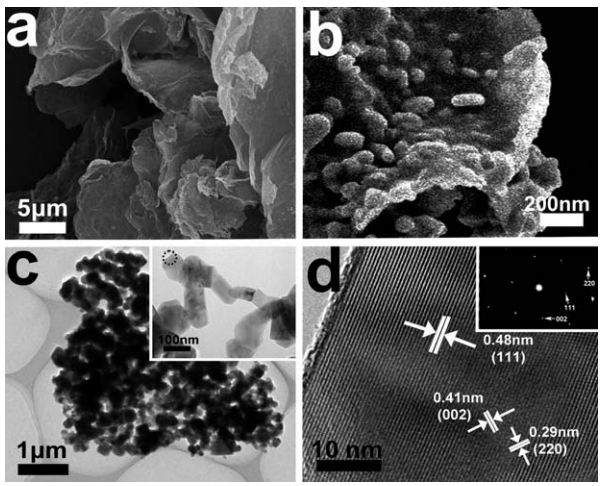

Fig. 2 (a) SEM image of porous $LiMn_2O_4$ nanosheets, (b) magnified SEM image of porous $LiMn_2O_4$ nanosheets, (c) TEM image of porous $LiMn_2O_4$ nanosheets (the inset shows a magnified TEM image), (d) HRTEM image corresponding to the circled area marked in the inset of Fig. 1c (the inset shows the corresponding SAED pattern).

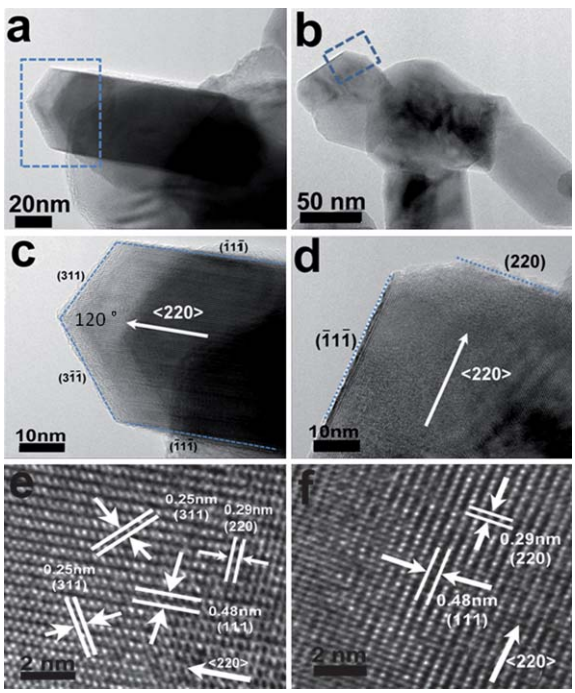

Fig. 3 (a and b) TEM images of randomly selected particles in $LiMn_2O_4$ nanosheets, (c) a magnified TEM image taken from the square area in (a), (d) a magnified TEM image taken from the circled area in (b), (e and f) HRTEM images corresponding to (c) and (d), respectively.

respectively. We highlight the edge of each $LiMn_2O_4$ particle in Fig. 3c and d. From the HR-TEM image (Fig. 3e), it evidently shows the lattice fringes of the {111}, {311}, and {220} planes of spinel-type $LiMn_2O_4$ nanorods. The highlighted area in Fig. 3c contains $(\bar{1}1\bar{1})$, (311), and $(3\bar{1}\bar{1})$ planes with crystallographic orientation of ⟨220⟩. The included angle by the (311) and $(3\bar{1}\bar{1})$ planes was measured to be about 120° which is in agreement with the value of the corresponding theoretical calculation. Meanwhile, Fig. 3f demonstrates that the highlighted area in Fig. 3d including the $(\bar{1}1\bar{1})$ and (220) planes has the same crystallographic orientation of ⟨220⟩, which suggests that the PS-LMO cathode has exposed {111} facets and the growth direction might be oriented along the ⟨220⟩ crystal directions. The electrode stability of $LiMn_2O_4$ depends on the reaction rate of SEI formation and the stability of the reconstructed surface structure, and {111} facets are more favorable in formation of SEI on the surface of $LiMn_2O_4$ which facilitates Li^+ ions insertion/desertion.[31] On this account, we expected that the PS-LMO cathode with exposed {111} facets could be used to provide better stability of the $LiMn_2O_4$ cathode against structural and volume change. Furthermore, the HRTEM images (Fig. 3e and f) clearly illustrate the atom arrangements, respectively, confirming that the $LiMn_2O_4$ nanosheets are single-crystalline, which will help to improve the electrochemical performance of PS-LMO, because single-crystalline cathodes contain fewer defects and show higher structural stability compared to poly-crystalline cathodes.[32]

In order to further test the electrochemical performance of PS-LMO, a coin-type half cell configuration was used in the lithium-ion batteries based on PS-LMO cathodes using Li metal as the anode. Representative charge-discharge curves of the PS-LMO at a rate of 120 mA g^{-1} (1C rate) between the voltage limits of 3.2–4.3 V are shown in Fig. 4a (first cycle). It can be seen that both the charge and discharge curves exhibited two plateaus at about 4.1 and 4.0 V *vs.* Li/Li^+, indicating a two-step process during cycling.[25] The two-step processes correspond to the two pairs of redox peaks in the CV plots (inset in Fig. 4a). The battery based on PS-LMO revealed a first charge capacity of about 116 mAh g^{-1}, and the discharge capacity is about 115 mAh g^{-1} with a coulombic efficiency of nearly 99%.

The cycle performance of PS-LMO and solid-state $LiMn_2O_4$ (denoted as SS-LMO) electrodes tested at a rate of 1C between potential limits of 3.2 and 4.3 V are shown in Fig. 4b. A slight increase in discharge capacity can be seen between the first and subsequent cycles, which can be attributed to the tendency of stabilization of PS-LMO after several cycles. Significantly, the discharge capacity remained unchanged after 500 cycles, indicating a 100% retention of the first discharge capacity. To the best of our knowledge, it is the best cycling performance reported for $LiMn_2O_4$ cathodes. In comparison, SS-LMO only keeps 86% of the initial capacity after 100 cycles and degrades quickly after further cycling. Differences in the capacity retention on cycling are reflected in the superior structural stability and lower Mn dissolution of PS-LMO compared with SS-LMO, which suggest that a two-dimensional nanosheet structure would alleviate the structural instability problem in $LiMn_2O_4$-based cathode materials[33] and PS-LMO may possess a stabilized surface that inhibits dissolution.[31] Besides, the nanoporous structure could act as a buffer layer to alleviate the volume

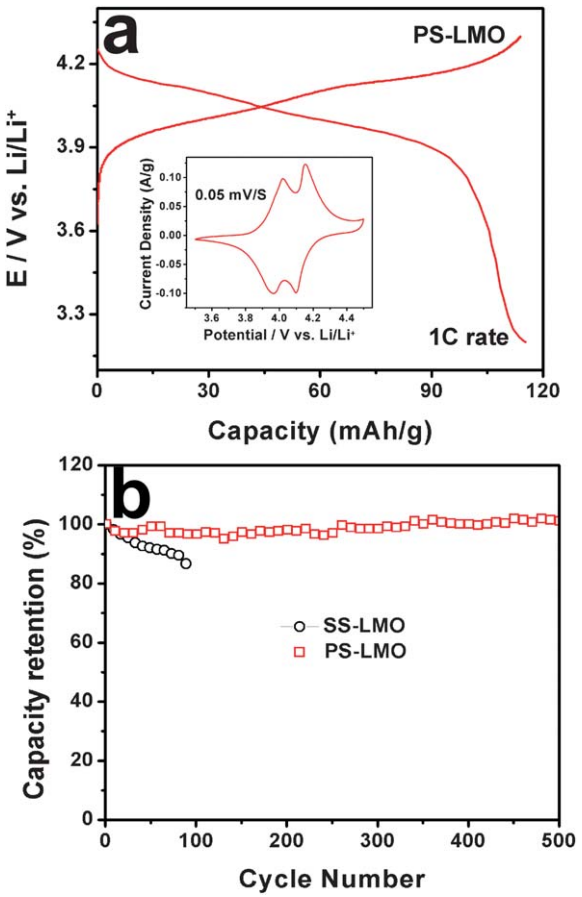

Fig. 4 (a) The first charge/discharge profiles of PS-LMO at 1C, inset: CV plot at 0.05 mV s^{-1}, (b) variation of discharge capacities *versus* cycle number for PS-LMO and SS-LMO cycled between voltage limits of 3.2 and 4.3 V at a current rate of 1C.

expansion of the electrode during lithiation/delithiation.[27] The rate capability performance, especially at a high rate, is another important aspect for the application of manganese-based spinel cathodes for high-power applications besides the cycling performance.

Fig. 5a shows a comparison of the rate capability between PS-LMO and SS-LMO during cycling at different discharge rates, varying from 1C to 25C. The discharge capacities of PS-LMO are much higher than those of SS-LMO. Additionally, with increasing current rate, the discharge capacities of the two materials decrease gradually, indicating the diffusion-controlled kinetic process for the electrode reactions of $LiMn_2O_4$ materials.[34] The discharge capacity of the PS-LMO cathode decreases to 115, 102, 96, 90, 82, and 69 mAh g^{-1}, when the current rate increases to 1, 3, 5, 8, 15, and 25C, respectively (see Fig. 5b). However, PS-LMO demonstrates an obviously lower fading rate with increasing discharge rates, revealing the good reversibility of PS-LMO during the Li^+ ion intercalation/deintercalation process. At 25C, PS-LMO could keep about 61% of its capacity compared with that at a rate of 1C, which is much higher than that of SS-LMO at the same rate (about 29%). This result shows that the role played by the 2D nanoporous structure of $LiMn_2O_4$ may facilitate the fast transport and intercalation kinetics of lithium ions. Namely, a rapid charge/discharge process will be

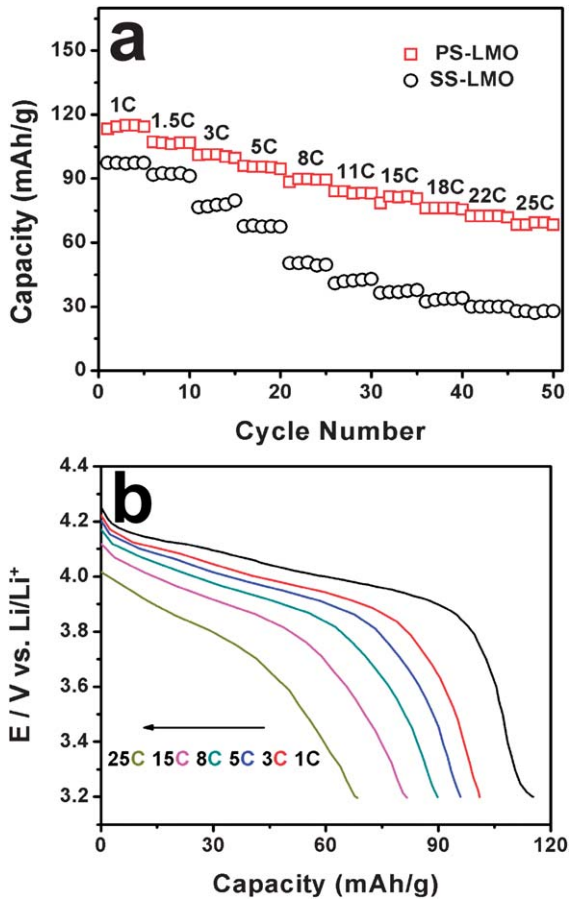

Fig. 5 (a) Variation in discharge capacities *versus* cycle number for PS-LMO and SS-LMO cycled at different current rates between voltage limits of 3.2 and 4.3 V, (b) discharge curves of PS-LMO at different discharge rates between voltage limits of 3.2 and 4.3 V.

completed in a very short time, resulting in a high specific capacity, even at a high charge-discharge current.

The rate capacity of PS-LMO was also investigated at a higher rate for 500 cycles. Even after 500 cycles at a high charge/discharge rate of 25C, approximately 86% of its initial capacity and 100% of its coulombic efficiency can still be retained (Fig. 6), revealing an excellent cycling performance at relatively high charge rates. To date, few papers have reported $LiMn_2O_4$ with this cycling performance at such a high discharge current. This is in agreement with the fact that PS-LMO can deliver admirable cycling stability attributed to its porous 2D nanosheet nature, which can timely relieve the strain and remit volume expansion/contraction caused by repeated Li^+ ion intercalation/deintercalation into/from the $LiMn_2O_4$ matrix.

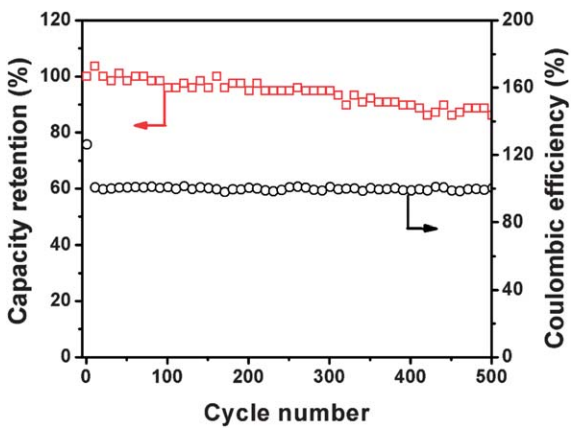

Fig. 6 Discharge capacity retention and coulombic efficiency as a function of cycle number for PS-LMO at 25C rate.

Conclusions

In summary, a template-free synthesis of PS-LMO with high porosity and crystallinity *via* calcinations of MnO_2 nanosheets coated with LiOH was achieved. This nanoporous two-dimensional (2D) framework exhibited superior cycling performance and a high-rate property compared with that of SS-LMO. The durable cycling performance was attributed to the intrinsic nanoporous nature of PS-LMO, high crystallinity, and exposed {111} facets that mitigated the structural instability during the lithiation of $LiMn_2O_4$ cathode materials, thus leading to fast Li-intercalation kinetics and excellent structural stability. Therefore, this PS-LMO electrode could be an ideal cathode candidate for high-power applications in rechargeable lithium-ion batteries.

Acknowledgements

This project was funded by The Hong Kong Polytechnic University Grant Research Committee Research Fund (Grant no. A-PD1T).

Notes and references

1 Z. Yang, J. Zhang, M. C. W. Kintner-Meyer, X. Lu, D. Choi, J. P. Lemmon and J. Liu, *Chem. Rev.*, 2011, **111**, 3577.
2 L. Ji, Z. Lin, M. Alcoutlabi and X. Zhang, *Energy Environ. Sci.*, 2011, **4**, 2682–2699.
3 J. Liu, G. Cao, Z. Yang, D. Wang, D. Dubois, X. Zhou, G. L. Graff, L. R. Pederson and J. G. Zhang, *ChemSusChem*, 2008, **1**, 676–697.
4 H. Li, Z. Wang, L. Chen and X. Huang, *Adv. Mater.*, 2009, **21**, 4593–4607.
5 C. M. Doherty, R. A. Caruso and C. J. Drummond, *Energy Environ. Sci.*, 2010, **3**, 813–823.
6 O. K. Park, Y. Cho, S. Lee, H. C. Yoo, H. K. Song and J. Cho, *Energy Environ. Sci.*, 2011, **4**, 1621.
7 P. G. Bruce, B. Scrosati and J. M. Tarascon, *Angew. Chem., Int. Ed.*, 2008, **47**, 2930–2946.
8 J. Tarascon, W. McKinnon, F. Coowar, T. Bowmer, G. Amatucci and D. Guyomard, *J. Electrochem. Soc.*, 1994, **141**, 1421.
9 S. H. Lim and J. Cho, *Electrochem. Commun.*, 2008, **10**, 1478–1481.
10 M. M. Thackeray, Y. Shao-Horn, A. J. Kahaian, K. D. Kepler, E. Skinner, J. T. Vaughey and S. Hackney, *Electrochem. Solid-State Lett.*, 1998, **1**, 7–9.
11 X. Wang, H. Nakamura and M. Yoshio, *J. Power Sources*, 2002, **110**, 19–26.
12 G. Nazri and G. Pistoia, *Lithium Batteries: Science and Technology*, Springer, The Netherlands, 2004.
13 L. Hernan, J. Morales, L. Sanchez, E. R. Castellon and M. Aranda, *J. Mater. Chem.*, 2002, **12**, 734–741.
14 K. M. Shaju and P. G. Bruce, *Chem. Mater.*, 2008, **20**, 5557–5562.
15 J. Gnanaraj, V. Pol, A. Gedanken and D. Aurbach, *Electrochem. Commun.*, 2003, **5**, 940–945.
16 D. Arumugam and G. Paruthimal Kalaignan, *Mater. Res. Bull.*, 2010, **45**, 1825–1831.
17 F. Jiao, J. Bao, A. H. Hill and P. G. Bruce, *Angew. Chem.*, 2008, **120**, 9857–9862.

18 Y. Wang and G. Cao, *Adv. Mater.*, 2008, **20**, 2251–2269.
19 Y. G. Guo, J. S. Hu and L. J. Wan, *Adv. Mater.*, 2008, **20**, 2878–2887.
20 D. K. Kim, P. Muralidharan, H. W. Lee, R. Ruffo, Y. Yang, C. K. Chan, H. Peng, R. A. Huggins and Y. Cui, *Nano Lett.*, 2008, **8**, 3948–3952.
21 X. W. Lou, Y. Wang, C. Yuan, J. Y. Lee and L. A. Archer, *Adv. Mater.*, 2006, **18**, 2325–2329.
22 D. Liu and G. Cao, *Energy Environ. Sci.*, 2010, **3**, 1218–1237.
23 B. Peng and J. Chen, *Coord. Chem. Rev.*, 2009, **253**, 2805–2813.
24 Y. Wang, K. Takahashi, K. H. Lee and G. Cao, *Adv. Funct. Mater.*, 2006, **16**, 1133–1144.
25 Y. L. Ding, X. B. Zhao, J. Xie, G. S. Cao, T. J. Zhu, H. M. Yu and C. Y. Sun, *J. Mater. Chem.*, 2011, **21**, 9475–9479.
26 H. Uchiyama, E. Hosono, H. Zhou and H. Imai, *J. Mater. Chem.*, 2009, **19**, 4012–4016.
27 F. Cheng, H. Wang, Z. Zhu, Y. Wang, T. Zhang, Z. Tao and J. Chen, *Energy Environ. Sci.*, 2011, **4**, 3668.
28 J. Luo, Y. Wang, H. Xiong and Y. Xia, *Chem. Mater.*, 2007, **19**, 4791–4795.
29 C. Wang, Y. Zhou, M. Ge, X. Xu, Z. Zhang and J. Jiang, *J. Am. Chem. Soc.*, 2010, **132**, 46–47.
30 C. Yuan, L. Hou, L. Yang, D. Li, L. Shen, F. Zhang and X. Zhang, *J. Mater. Chem.*, 2011, **21**, 16035–16041.
31 M. Hirayama, H. Ido, K. S. Kim, W. Cho, K. Tamura, J. Mizuki and R. Kanno, *J. Am. Chem. Soc.*, 2010, **132**, 15268–15276.
32 Y. Liu, B. Chen, F. Cao, X. Zhao and J. Yuan, *J. Mater. Chem.*, 2011, **21**, 10437–10441.
33 D. Rangappa, D. Murukanahally, T. Tomai, A. Unemoto and I. Honma, *Nano Lett.*, 2012, **12**, 1146–1151.
34 C. J. Curtis, J. Wang and D. L. Schulz, *J. Electrochem. Soc.*, 2004, **151**, A590.